Link between supercurrent diode and anomalous Josephson effect revealed by gate-controlled interferometry

S. Reinhardt,[1] T. Ascherl,[1] A. Costa,[2] J. Berger,[1] S. Gronin,[3] G. C. Gardner,[3]
T. Lindemann,[3,4] M. J. Manfra,[3,4,5,6] J. Fabian,[2] D. Kochan,[7,2] C. Strunk,[1] and N. Paradiso[1, *]

[1]*Institut für Experimentelle und Angewandte Physik, University of Regensburg, 93040 Regensburg, Germany*
[2]*Institut für Theoretische Physik, University of Regensburg, 93040 Regensburg, Germany*
[3]*Birck Nanotechnology Center, Purdue University, West Lafayette, Indiana 47907 USA*
[4]*Department of Physics and Astronomy, Purdue University, West Lafayette, Indiana 47907 USA*
[5]*School of Materials Engineering, Purdue University, West Lafayette, Indiana 47907 USA*
[6]*Elmore Family School of Electrical and Computer Engineering,*
Purdue University, West Lafayette, Indiana 47907 USA
[7]*Institute of Physics, Slovak Academy of Sciences, 84511 Bratislava, Slovakia*

In Josephson diodes the asymmetry between positive and negative current branch of the current-phase relation leads to a polarity-dependent critical current and Josephson inductance. The supercurrent nonreciprocity can be described as a consequence of the anomalous Josephson effect —a φ_0-shift of the current-phase relation— in multichannel ballistic junctions with strong spin-orbit interaction. In this work, we simultaneously investigate φ_0-shift and supercurrent diode efficiency on the same Josephson junction by means of a superconducting quantum interferometer. By electrostatic gating, we reveal a direct link between φ_0-shift and diode effect. Our findings show that the supercurrent diode effect mainly results from magnetochiral anisotropy induced by spin-orbit interaction in combination with a Zeeman field.

I. INTRODUCTION

In solids, spin-orbit interaction (SOI) makes it possible to control orbital degrees of freedom by acting on the electron spin, and vice-versa [1, 2]. In superconductors [3], the impact of SOI can be particularly spectacular, since it enables phenomena which go beyond the realm of conventional *s*-wave superconductors, as e.g. topological phases [4], finite-momentum superconductivity [5–7], Lifshitz invariant [8–10], Ising superconductivity [11], anomalous Josephson effect [12–16] and intrinsic supercurrent diode effect [17–31]. In what follows, we shall focus on the last two effects and on their relation in Josephson junctions.

The anomalous Josephson effect manifests itself in a phase offset φ_0 at zero current, $I(\varphi_0) = 0$, in the current-phase relation (CPR) [15, 16, 32–36]. This also implies a finite supercurrent at zero phase difference $I(\varphi = 0) \neq 0$. The effect requires the simultaneous breaking of both inversion and time-reversal symmetry [37], which can be provided by SOI and Zeeman field, respectively.

The same symmetries need to be broken in order to observe the supercurrent diode effect (SDE), namely, the dependence of the critical current on the bias polarity. This effect can be trivially obtained, e.g., in asymmetric superconducting quantum interference devices (SQUIDs) [38] or, more generally, when in a film an inhomogeneous supercurrent distribution is coupled to a flux. Recently, it was shown [17–19, 22–27, 30, 31] that supercurrent rectification can as well emerge as an intrinsic feature of *homogeneous* quasi-2D systems subjected to a Zeeman field. Such nontrivial SDE is a new precious probe of the condensate physics (in films) [10] and of Andreev bound states (ABSs) in Josephson junctions [27, 30], including possible topological properties [39–41].

Several mechanisms have been proposed to explain such intrinsic SDE in films [10, 42–46] and Josephson junctions [47–53]. In superconducting-normal-superconducting (SNS) junctions the supercurrent can be computed in terms of the ABSs in the N weak link. In experiments, ABSs can be directly probed by tunnel spectroscopy [36, 54, 55], while their effect on the CPR can be deduced from IV-characteristics, inductance versus current measurements [18, 27, 56] and SQUID experiments [57].

Early observations on Josephson diodes were interpreted in terms of φ_0-shift in ballistic systems with skewed CPR [18, 22–24, 56]. Within this picture, the SDE ultimately originates (as it does the φ_0-shift) from SOI. An alternative model, proposed by Banerjee *et al.* [30] based on the theory of Ref. [50], explains the same effect in terms of a purely orbital mechanism. To date, it is not clear yet to which extent the two mechanisms (namely, the SOI-based and the purely orbital mechanism) contribute to the supercurrent rectification observed in experiments.

In this work, we make use of an asymmetric SQUID with mutually orthogonal junctions to directly measure both the anomalous φ_0-shift and the SDE on the same junction. By gating, we can electrostatically control both effects and highlight their relation. Finally, by measuring the temperature dependence of the φ_0-shift and of the diode efficiency we demonstrate that the former is a necessary but not sufficient condition for the SDE. This latter requires in fact the presence of higher harmonics in the CPR, which are quickly suppressed by increasing the temperature. We comment on our results in light of alternative models proposed in the literature and compare the temperature dependence of φ_0 and the SDE to the predictions of a minimal theoretical model.

* nicola.paradiso@physik.uni-regensburg.de
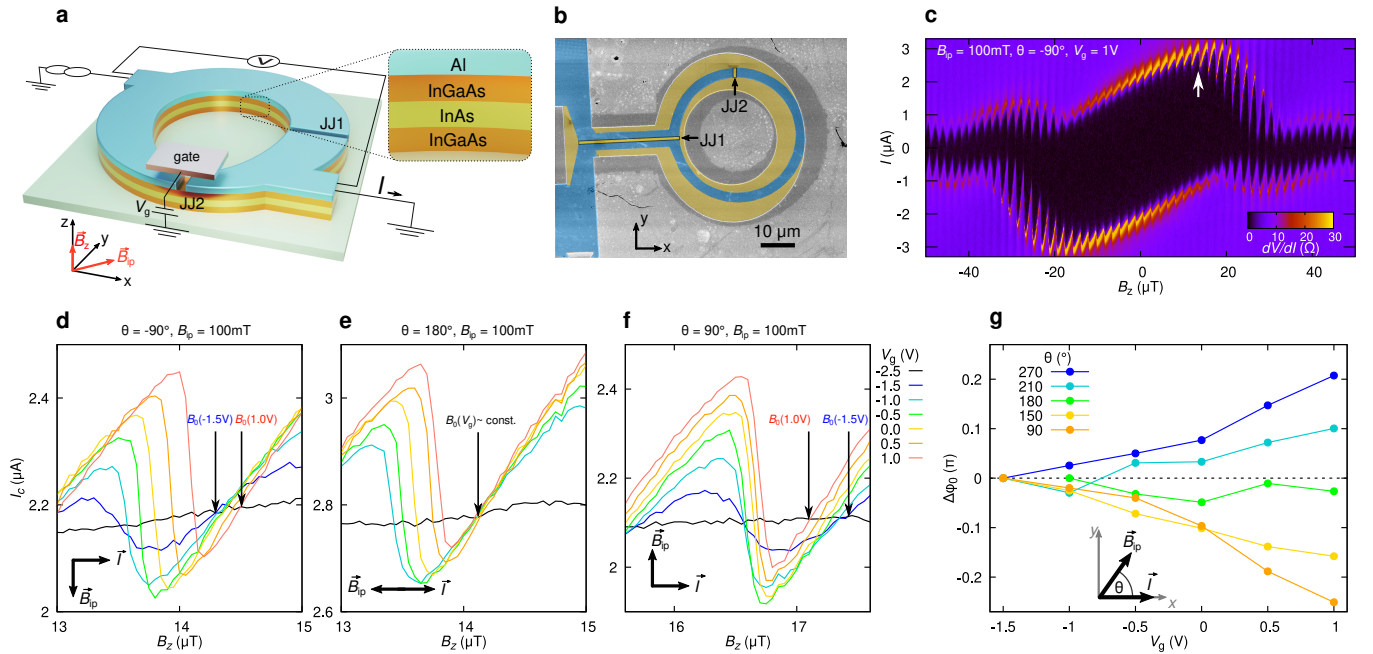
FIG. 1. **Asymmetric SQUID device with reference junction and gate-controllable φ_0 junction. a**, (Left) Schematic illustration of the device. The SQUID consists of a large reference junction (JJ1) and of a small junction (JJ2) which is coupled to a gate. By applying a magnetic field along $\hat{y}$, a φ_0-shift is induced in the CPR of the latter junction, which can be controlled by electrostatic gating. (Right) Scheme of the topmost layers of the heterostructure. The black arrow indicates the direction of the positive current bias I. **b**, False-color scanning electron microscopy image of the device taken before gate patterning. The pristine superconducting Al/InAs leads are highlighted in turquoise, the areas where Al is selectively etched in yellow (including the weak links, highlighted by the black arrows). The remaining parts in gray correspond to deeply etched regions, where both the Al film and the topmost semiconducting layers are etched. **c**, The color plot shows the SQUID differential resistance versus out-of-plane field B_z and current I, for $\theta = -90°$ and $B_{\mathrm{ip}} = 100$ mT (i.e., $B_x = 0$, $B_y = -100$ mT) at $T = 40$ mK. The white arrow indicates where anomalous phase shifts were measured (see panels **d-f**). **d**, SQUID critical current I_c as a function of B_z, for θ and B_{ip} as in **c**. The different curves refer to different gate voltages V_g. We define $B_0(V_g)$ as the crossing of each curve with the $V_g = -2.5$ V reference curve (black). **e** and **f**, Corresponding measurements for the same $B_{\mathrm{ip}} = 100$ mT but, respectively, $\theta = 180°$ and $\theta = 90°$. **g**, Plot of $\Delta\varphi_0(V_g) \equiv 2\pi A[B_0(V_g) - B_0(V_g = -1.5 \text{ V})]/\Phi_0$, for different $\vec{B}_{\mathrm{ip}}$ orientations, i.e., for different θ. Here, A is the loop area and Φ_0 the flux quantum.

II. DEVICE DESCRIPTION AND EXPERIMENTAL RESULTS

Figure 1**a** shows a scheme of our SQUID. The device is fabricated starting from a molecular beam epitaxy-grown heterostructure featuring an InGaAs/InAs/InGaAs quantum well, capped by a 5 nm-thick epitaxial Al film [18, 58–60]. The quantum well hosts a 2D electron gas (2DEG) with a proximity-induced superconducting gap inherited from the Al film. By deep wet etching, we define an asymmetric SQUID loop. The actual geometry is shown in the false-color scanning electron microscopy image in Fig. 1**b**, where the turquoise areas indicate the pristine Al/InGaAs/InAs/InGaAs regions, while the gray areas refer to deeply etched (insulating) regions. To obtain the two normal (N) weak links, we selectively etch the Al film (yellow areas in Fig. 1**b**). The reference Josephson junction 1 (JJ1) is 28 µm-wide and 120 nm-long, whereas the Josephson junction 2 (JJ2) is 2.7 µm-wide and 100 nm-long. Finally, a gate is fabricated on top of JJ2, which allows us to control the electron density in the N-link and thus the critical current $I_{c,2}$ of this junction. The two junctions are mutually

perpendicular, so that an in-plane magnetic field $\vec{B}_{\mathrm{ip}}$ parallel to the short junction, i.e., along $\hat{y}$, (see Fig. 1**a,b**) will induce magnetochiral effects [18] in the short junction only, and not in the reference junction. Here, we take as positive $\hat{z}$ direction that perpendicular to the 2DEG and directed from the substrate towards the Al (see Fig. 1**a**), which corresponds to the direction opposite to the built-in electric field in the quantum well [18, 61] which provides SOI in the 2DEG [18, 61].

We measure differential resistance in a 4-terminal geometry as a function of DC current. In what follows, we indicate as I_c the (measured) SQUID critical current (see Methods) and as $I_{c,i}$ ($i = 1, 2$) the (deduced) critical current in junction i. When needed, we use the superscript + (−) to indicate positive (negative) current from source to drain (see Fig. 1**a**), i.e., supercurrent in the positive (negative) x direction in JJ2. For the in-plane field, we interchangeably use either Cartesian components, or magnitude and angle parametrization, i.e. $\vec{B}_{\mathrm{ip}} = B_x\hat{x} + B_y\hat{y} = B_{\mathrm{ip}}(\cos\theta, \sin\theta)$, see cartesian axes in Fig. 1**a**.

Figure 1**c** shows the color plot of the differential resistance versus out-of-plane field B_z and DC current I, measured with

an applied field $B_y = -100$ mT at $T = 40$ mK. The fast oscillations have period 1.8 µT, corresponding to a flux quantum $\Phi_0 = h/2e$ applied to the loop. Such oscillations are superimposed to the Fraunhofer pattern of the reference junction, whose central and first side lobes are visible. The plot displays an evident asymmetry around the $B_z = 0$ and $I = 0$ axes, while it is approximately point-inversion-symmetric around the origin, namely $I_c(B_z) \approx -I_c(-B_z)$. As discussed in the Supplementary Information, such asymmetry is due to screening effects, which arise when there are current-dependent corrections to the fundamental SQUID relation

$$\gamma_1 - \gamma_2 = \frac{2\pi}{\Phi_0}\Phi, \tag{1}$$

where γ_i it the gauge-invariant phase drop at the i-th junction, Φ_0 is the flux quantum and Φ the flux through the loop. The corrections originate either from the additional flux induced by the SQUID current itself, or by the phase drop accumulated along the loop arms [38, 62]. The former correction is proportional to the geometric loop inductance, while the latter is proportional to the kinetic inductance of the SQUID arms [63]. As discussed in the Methods, in our sample, screening is mostly dominated by the large kinetic inductance of the thin Al film, whose sheet inductance is $L_\square \sim 30$ pH. The geometric loop inductance is comparatively small, see Supplementary Information. As shall be discussed below, screening effects hinder the measurement of both the absolute value of the anomalous shift φ_0 and that of the diode efficiency. Indeed, the determination of the absolute φ_0 is challenging even in SQUID devices with low screening and reference devices [32, 36]. One of the difficulties is the fact that an accurate determination of φ_0 requires a reproducible B_z control on the microtesla scale, while an in-plane field of the order of tens or hundreds of millitesla is swept.

The determination of the *absolute* φ_0 is usually difficult in systems with large kinetic inductance. Similar to Refs. [33, 34, 36], we shall measure the *relative* shift of the CPR with respect to that for large negative gate voltage. Figure 1d shows SQUID oscillations measured for different gate voltages V_g. The measurement is performed with an in-plane field $B_{\text{ip}} = 100$ mT applied perpendicular to JJ2 ($\theta = -90°$) at $T = 40$ mK. The oscillations are taken near the maximum of the tilted Fraunhofer pattern, indicated by the upper arrow in Fig. 1c. The black curve ($V_g = -2.5$ V) refers to a completely pinched-off JJ2 ($I_{c,2} = 0$), and serves as zero-current baseline. The first curve for which oscillations are clearly visible is that for $V_g = -1.5$ V. We shall label as $B_0(V_g)$ the crossing with positive slope of each $I_c(V_g)$ curve with the baseline $I_c(V_g = -2.5$ V), see Fig. 1d. As discussed in the Supplementary Information, at these crossings the supercurrent I_2 in JJ2 vanishes, therefore its gauge invariant phase difference is, by definition, the anomalous shift φ_0. We consider variations of φ_0 with respect to the reference voltage $V_g = -1.5$ V [36], namely, $\Delta\varphi_0 \equiv 2\pi A_{\text{loop}}[B_0(V_g) - B_0(V_g = -1.5$ V)]/Φ_0, where $A_{\text{loop}} = 1150$ µm^2 is the loop area.

Figures 1e and 1f show the results of the same measurements after two subsequent -90° sample rotation, namely, for $\theta = 180°$ and $\theta = 90°$, respectively. From Fig. 1e we deduce

that for $\vec{B}_{\text{ip}} \parallel \vec{I}$, the curves crosses the baseline with positive slope nearly at the same B_z (i.e., $B_0(V_g)$ is constant). Instead, for $\vec{B}_{\text{ip}} \perp \vec{I}$, $B_0(V_g)$ monotonically increases (decreases) with V_g for negative (positive) sign of $\hat{e}_z \cdot (\vec{B}_{\text{ip}} \times \vec{I})$. This is a clear signature of the magnetochiral nature of the anomalous Josephson effect [18].

The variation of $\Delta\varphi_0(V_g)$ for different $\vec{B}_{\text{ip}}$ orientations (i.e., for different θ with $|\vec{B}_{\text{ip}}| = 100$ mT) is plotted in Fig. 1g. We stress that, since we subtract $\varphi_0(V_g = -1.5$V) (as in the definition of $\Delta\varphi_0$), what is important in Fig. 1g is the monotonic increase or decrease of $\Delta\varphi_0$ with the gate voltage. The graph clearly shows the proportionality of $\Delta\varphi_0$ to [18] $-\hat{e}_z \cdot (\vec{B}_{\text{ip}} \times \vec{I})$, as expected by SOI-based models for the anomalous Josephson effect [12]. For all curves, the magnitude of $|\Delta\varphi_0|$ increases with V_g. The monotonic increase is expected, since in this type of InGaAs/InAs/InGaAs quantum wells, a positive gate voltage increases the built-in electric field [61] responsible for the Rashba SOI [18, 61].

The main goal of our experiments is to establish a relation between the anomalous φ_0-shift and intrinsic SDE by measuring both phenomena *on the same junction*. For this purpose, we investigate SQUID oscillations for both current bias polarities in order to deduce both the positive ($I_{c,2}^+$) and the negative ($I_{c,2}^-$) critical current of JJ2. Figure 2a shows the SQUID interference pattern measured in the vicinity of $B_z = 0$ for $B_y = -50$ mT at $V_g = 1.0$ V (red), together with the reference curve at $V_g = -2.5$ V (black, where $I_{c,2} = 0$ and SQUID oscillations vanish). Figure 2b shows several $I_c^+(B_z)$ curves for different gate voltages V_g, measured at $B_y = -50$ mT and $T = 40$ mK, as in Fig. 2a. We focus on one particular oscillation highlighted by the upper arrow in Fig. 2a. The corresponding I_c^- curves for the opposite B_z range (lower arrow in Fig. 2a) are shown in panel c. We use the baseline curve in Fig. 2a (black, $V_g = -2.5$ V) as a reference to extract $I_{c,2}^+$ from data in Fig. 2b and $I_{c,2}^-$ from Fig. 2c. For each V_g, $I_{c,2}^+$ corresponds to the maximum in B_z (see red arrow in Fig. 2b) of the difference $I_c^+(B_z, V_g) - I_c^+(B_z, V_g = $ -2.5 V). $I_{c,2}^-$ is deduced in a similar way from $I_c^-(B_z, V_g) - I_c^-(B_z, V_g = $ -2.5 V).

The resulting $I_{c,2}^+(V_g)$ and $I_{c,2}^-(V_g)$ are plotted in Fig. 2d. As a figure of merit for the supercurrent rectification, we use the supercurrent diode efficiency $\eta \equiv (I_{c,2}^+ - |I_{c,2}^-|)/\langle I_{c,2}\rangle$, with $\langle I_{c,2}\rangle \equiv (I_{c,2}^+ + |I_{c,2}^-|)/2$. The efficiency $\eta(V_g)$ is plotted in Fig. 2e for different values of B_y in the different subpanels (i-v). As explained in the Supplementary Information, owing to SQUID screening effects η is affected by trivial offset, which means that data in Figs. 2e might be subjected to a spurious vertical shift. Nevertheless, the *variation* of η when V_g is swept remains unaffected by screening artifacts. Since the modulation of η with V_g is roughly proportional to η itself, we use $\partial\eta/\partial V_g$ as a measure of η. In particular, we expect that the slope $\partial\eta/\partial V_g$ must display the same magnetochiral behavior as η itself. Data in Fig. 2e(i-v) show that $\partial\eta/\partial V_g$ is linear in B_y, similar to the rectification efficiency η reported in single Josephson junctions from similar materials [18, 22, 24, 25]. The complete overview of the B_y-dependence of $\partial\eta/\partial V_g$ is shown in Fig. 2f. As in previous reports on Josephson diodes, the rectification efficiency is linear in B_y only up to a certain
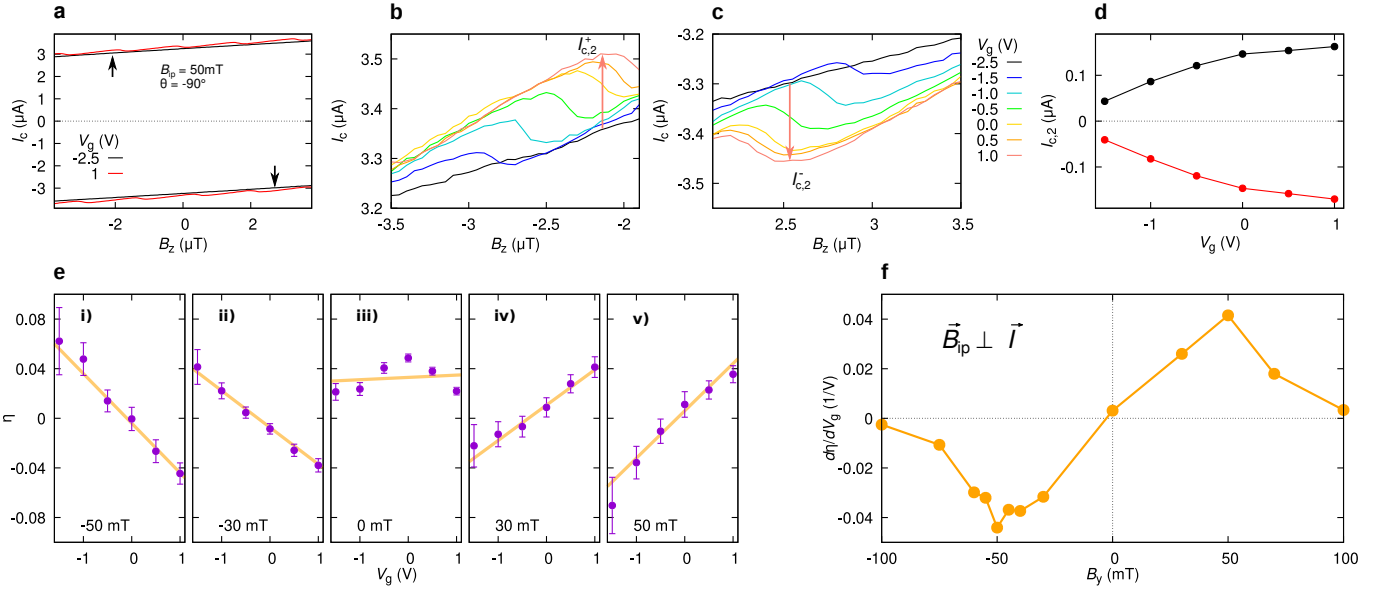
FIG. 2. **Gate control of the supercurrent diode effect. a**, Positive and negative SQUID critical current for an out-of-plane field B_z close to zero, $T = 40$ mK, and $B_y = -50$ mT. The red (black) curve refers to a gate voltage $V_g = 1.0$ V ($V_g = -2.5$ V). The upper and lower arrow indicates the oscillation highlighted in panel **b** and **c**, respectively. They are located asymmetrically in B_z, eliminating the trivial diode effect of the background. **b**, Positive critical current I_c^+ versus out-of-plane field B_z. The red arrow indicates $I_{c,2}^+$ for the $V_g = 1$ V-curve, see text. **c**, Negative critical current I_c^- versus B_z. The red arrow indicates $I_{c,2}^+$ for the $V_g = 1$ V-curve. The different curves in **b** and **c** correspond to different values of the gate voltage V_g. Measurements are performed at $T = 40$ mK and $B_y = -50$ mT. **d**, $I_{c,2}^+$ and $I_{c,2}^-$ versus V_g for $B_y = -50$ mT. **e**, Diode efficiency $\eta \equiv 2(I_c^+ - |I_c^-|)/(I_c^+ + |I_c^-|)$ versus V_g, for $B_y = -50$ mT (i), -30 mT (ii), 0 mT (iii), 30 mT (iv), 50 mT (v). **f**, Slope of the diode efficiency $d\eta/dV_g$, plotted versus B_y.

threshold (here at $|B_y| = 50$ mT): after that, a clear suppression is observed [27].

The results shown so far provide strong evidence of the link between anomalous phase shift and SDE. Both effects are linear in B_y. Both $\Delta\varphi_0$ and η can be modulated by a gate voltage in the accessible range $V_g \in$[-1.5 V, 1.0 V]. This is consistent with the SOI-based model [10, 18, 24, 53, 56] of the SDE, where the supercurrent rectification is accompanied by the anomalous Josephson shift φ_0. The φ_0-shift is a necessary but not sufficient condition for the supercurrent nonreciprocity. To break the symmetry between positive and negative part of the CPR, multiple ballistic channels are needed [14, 27]. In finite-width junctions with parabolic dispersion, each i-channel has a different $\varphi_{0,i}$-shift, owing to the different Fermi velocity $v_{F,i}$: in fact, for a single ballistic channel, $\varphi_{0,i} \propto v_{F,i}^{-2}$ [12]. The total CPR is the sum of all single-channel CPR contributions $I_i(\varphi + \varphi_{0,i})$. The sum of skewed CPRs with different $\varphi_{0,i}$-shift leads to an asymmetric total CPR, whose positive and negative branch are different. The skewness (i.e., the content of higher harmonics) of the individual CPRs is crucial, since otherwise the sum of sinusoidal CPRs would always lead to a sinusoidal –i.e., reciprocal– CPR. The relation between η and φ_0 is evident from the comparison between Fig. 1**g** and Fig. 2**e**. On the other hand, since the SDE also relies on the presence of higher harmonics in the CPR [18], we expect that η (and thus $\partial\eta/\partial V_g$) will be highly sensitive to the junction transparency and temperature, as opposed to the anomalous shift φ_0.

Figures 3**a** and 3**b** respectively show the temperature dependence of φ_0 and η as obtained from a simple theoretical model (described in Methods and in Refs. [27, 53]) for a Josephson junction in the short-ballistic limit with Zeeman interaction. The junction separates two semi-infinite superconducting 2DEGs with zero-temperature superconducting gap $\Delta^*(0) \approx 130\,\mu$eV [60], and critical temperature $T_c \approx 2$ K. We note that the anomalous shift φ_0 is nearly T-independent, whereas the supercurrent rectification is strongly suppressed already for $T > 100$ mK.

In Fig. 3**c** and 3**d** we show the measured temperature dependence of $\Delta\varphi_0$ and that of $\partial\eta/\partial V_g$, which we take as measures of $\varphi_0(T)$ and $\eta(T)$, respectively. $\Delta\varphi_0(T)$ is measured at $B_y = -100$ mT, ($B_{ip} = 100$ mT, $\theta = -90°$), where the field magnitude is set large enough to limit screening effects to an acceptable level. Instead, $\partial\eta/\partial V_g(T)$ is measured at $B_y = 50$ mT, where the SDE is maximal, see Fig. 2**f**. Figure 3**c** shows that $\Delta\varphi_0$ is temperature-independent within the experimental accuracy. In contrast, the (gate modulation of the) supercurrent rectification is clearly suppressed already at temperatures well below T_c, as shown in Fig. 3**d**. Both observations match the corresponding theory predictions.

A comment is in order about the sign and magnitude of the effects. Both our experimental data and analytical model show that if the Rashba SOI-inducing electric field is directed along $-\hat{z}$ (as in Ref. [61] and in the Supplementary Information of Ref. [18]), $\vec{B}_{ip}$ along $+\hat{y}$, and the positive current bias along $+\hat{x}$, then $\varphi_0 < 0$ [where $I(\varphi_0) = 0$, $\partial_\varphi I(\varphi_0) > 0$] and $\eta > 0$.
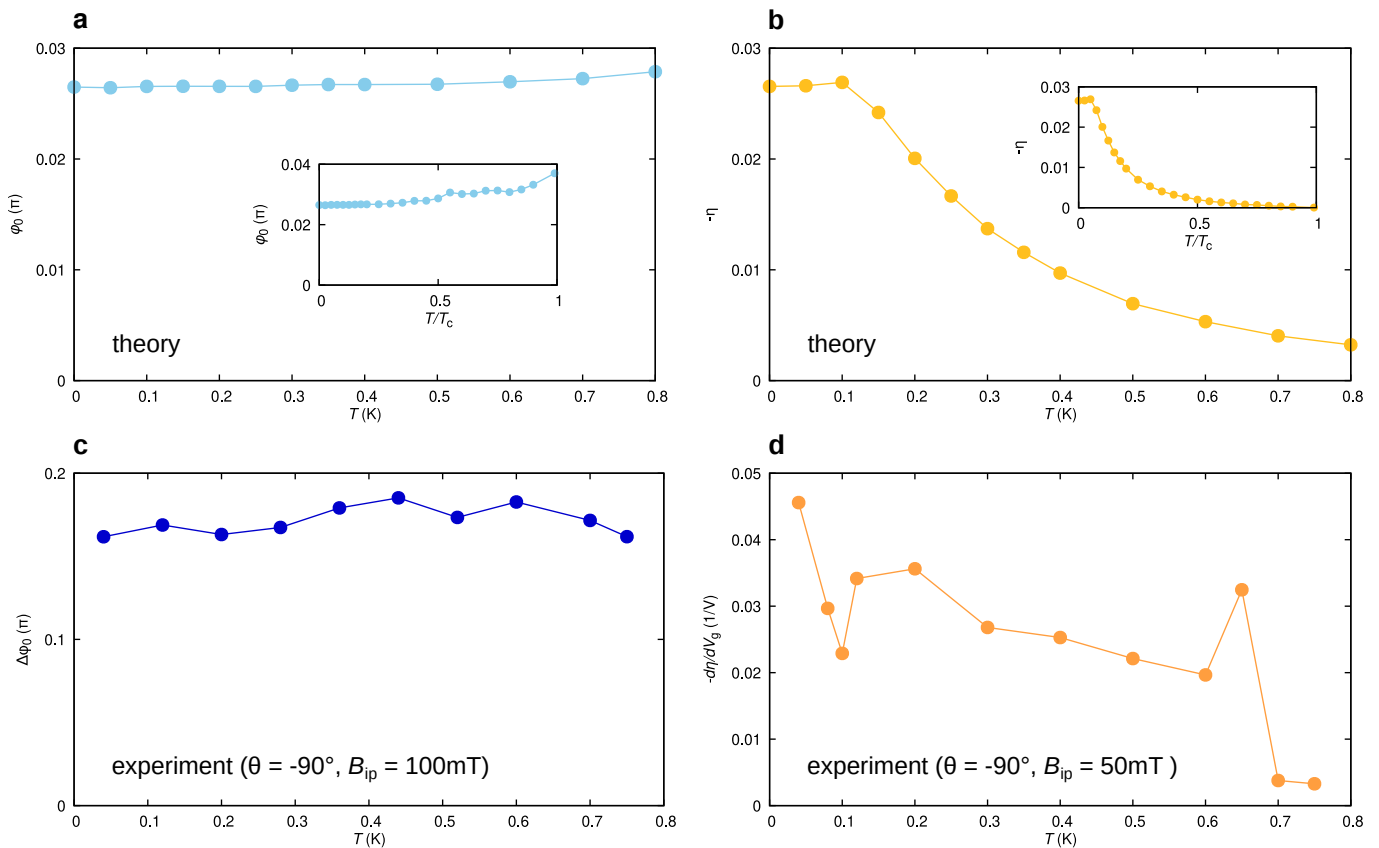
FIG. 3. **Temperature dependence of φ_0 and η: theory and experiment. a**, Computed temperature dependence of the (sign changed) anomalous phase shift φ_0 for a Zeeman parameter of $\lambda_Z = -0.40$ (which would correspond to $B_y = -100$ mT for g-factor $|g| = 12$). We assume $T_c = 2.0$ K as in the experiments. Inset: full-range $\varphi_0(T)$ graph plotted for T up to $T = T_c$. **b**, Computed temperature dependence of the supercurrent diode rectification efficiency $-\eta$ for the same parameters as in **a**. Inset: full-range $-\eta(T)$ graph up to $T = T_c$. **c**, Measured $\Delta\varphi_0$ (as defined in the text) at $V_g = 1.0$ V and $B_y = -100$ mT, plotted as a function of temperature. **d**, Temperature dependence of $d\varphi_0/dV_g$ (as defined in the text) at $B_y = 50$ mT. For ease of comparison, all main graphs are plotted up to $T = 0.8$ K, the highest temperature for which $\Delta\varphi_0$ and $d\varphi_0/dV_g$ was measurable.

Instead, the magnitude of φ_0 and η predicted by ballistic theory [12] is smaller than the one measured in our and in other experiments in the literature [32, 33]. A possible explanation for this discrepancy could be disorder in and near the junction [32], since diffusive models predict a much larger φ_0. Another possibility is the enhancement of SOI due to interaction of quantum well electrons with the image charges that are formed in a nearby Al gate. The nontrivial property of the induced image-potential that depends on the electron density of 2DEG gives a feedback on SOI that superimposes with the innate Rashba SOI of the quantum well without metallic gate as demonstrated in Refs. [64–66].

III. DISCUSSION

The main goal of our study is to elucidate the physical mechanism behind the intrinsic SDE in single, homogeneous Josephson junctions. The effect has been so far explained by two different models: one [14, 18, 56] is based on the combination of Rashba SOI plus Zeeman interaction (due to

an external in-plane field or exchange interaction); the other is a purely orbital mechanism [30, 50] based on the finite Cooper pair momentum induced in the superconducting leads by the flux associated to the in-plane field [30]. This flux is finite if the parent superconducting film and the 2DEG are spatially separated.

The main difference between the two pictures is the expected dependence on V_g. Such dependence naturally emerges since V_g affects the band alignment and thus the Rashba coefficient α_R. Both α_R and the electron density n critically affect φ_0, which, in turn, determines η in multichannel systems. In contrast, the orbital mechanism [30] hardly depends on the gate voltage [67]. As discussed in the Supplementary Information, the gate voltage also affects the magnetochiral anisotropy for the inductance [18], an effect that is strictly related to the supercurrent rectification [27]. The observed strong gate dependence of φ_0 and η indicates that the Rashba-based mechanism must certainly play an important role in the SDE. On the other hand, the orbital mechanism cannot be ruled out by our observations: it could still coexist with the spin-orbit-based mechanism.

Finally, we would like to stress that, even though we make use of a SQUID to link η to φ_0, our point does not concern the (trivial and long known [38]) SDE of the asymmetric SQUID as a whole. Our focus is exclusively on the intrinsic SDE in a single, homogeneous junction (JJ2).

In conclusion, we have shown the coexistence of anomalous Josephson effect and supercurrent rectification by measuring both effects on the same Josephson junction embedded in a SQUID. The observed gate voltage and temperature dependence are compatible with a spin-orbit based picture where supercurrent rectification arises in multichannel junctions with anomalous shift φ_0 *and* skewed current-phase relation.

Josephson diodes based on φ_0-junctions are important for both fundamental research and applications. They are novel and powerful probes of symmetry breaking in 2D superconductors [21, 49, 68] and possible probes of topological phase transitions [39]. A recent proposal [69] suggested that the anomalous Josephson effect might be used in multiterminal junctions to obtain compact nonreciprocal devices as, e.g., circulators for rf-applications [70].

IV. METHODS

A. Experimental methods

The heterostructure is grown by molecular beam epitaxy. The full layer sequence is reported in the Supplementary Information. The most relevant layers are the topmost ones, namely, the nominally 5 nm-thick Al film at the sample surface, a 10 nm thick $In_{0.75}Ga_{0.25}As$ layer acting as a barrier, a 7 nm InAs layer hosting the 2DEG, followed by another $In_{0.75}Ga_{0.25}As$ barrier of thickness 4 nm. Structures are defined by electron beam lithography. The selective etching of Al is performed by wet chemical etching using Transene D. Deep etching processes (where the 2DEG is removed altogether) is performed using a phosphoric acid-based solution.

Transport measurements are performed in a 4-point configuration using standard lock-in techniques. To determine the SQUID critical current I_c^+ and I_c^- as defined in the text we take $dV/dI = 6\,\Omega$ as a threshold.

To determine the correct offset for B_z we look at the symmetry of the plot of $R = dV/dI$ versus I and B_z, see e.g., Fig. 1c. Since $R(I, B_z) \approx R(-I, -B_z)$, the center of inversion symmetry of the plot allows us to determine the applied out-of-plane field which corresponds to an effective $B_z = 0$.

B. Theoretical methods

Our theoretical model, initially developed in Refs. [27, 53], describes the experimentally relevant system in terms of a short S–N–S Josephson junction that couples two semi-infinite s-wave superconducting (S) regions with inherently strong Rashba SOI through a thin delta-like normal-conducting (N) link. Nontrivial solutions of the 2D Bogoliubov–de Gennes equation [71]

$$\begin{bmatrix} \hat{\mathcal{H}} & \hat{\Delta}(x) \\ \hat{\Delta}^\dagger(x) & -\hat{\sigma}_y(\hat{\mathcal{H}})^*\hat{\sigma}_y \end{bmatrix} \Psi(x, y) = E\Psi(x, y), \quad (2)$$

with the single-electron Hamiltonian

$$\hat{\mathcal{H}} = \left[-\frac{\hbar^2}{2m}\left(\frac{\partial^2}{\partial x^2} + \frac{\partial^2}{\partial y^2} \right) - \mu \right] \hat{\sigma}_0 \\ + \alpha_R \left(k_y\hat{\sigma}_x - k_x\hat{\sigma}_y \right) \\ + \left(V_0\hat{\sigma}_0 + V_Z\hat{\sigma}_y \right) d\delta(x), \quad (3)$$

determine the energies E and wave functions $\Psi(x, y)$ of the Andreev bound states [72], which are at the heart of the coherent Cooper-pair supercurrent transport along the $\hat{x}$-direction; $\hat{\Delta}(x)$ corresponds to the s-wave superconducting pairing potential that we approximate by

$$\hat{\Delta}(x) = \Delta^*(T) \left[\Theta(-x) + e^{i\varphi}\Theta(x) \right], \quad (4)$$

where $\Delta^*(T) = \Delta^*(0)\tanh(1.74\sqrt{T_c/T - 1})$ is the temperature-dependent proximity-induced superconducting gap [from the experimental data, the induced gap at zero temperature was estimated as $\Delta^*(0) \approx 130\,\mu eV$ and the critical temperature as $T_c \approx 2\,K$] and φ indicates the phase difference between the two superconducting regions. The Rashba SOI that is present throughout the whole system is parameterized by α_R, V_0 and V_Z represent the scalar (spin-independent) and Zeeman (spin-dependent) potentials inside the delta-like N link of thickness d—the magnetic field causing the Zeeman splitting is thereby aligned perpendicular to the current direction (i.e., along $\hat{y}$)—, μ is the Fermi energy, m the (effective) quasiparticle mass, and $\hat{\sigma}_0$ and $\hat{\sigma}_i$ refer to the 2×2 identity and ith Pauli spin matrix, respectively.

After determining the Andreev-state energies $E(\varphi)$ as a function of the superconducting phase difference φ, we apply the quantum-mechanical current operator to the corresponding bound-state wave functions inside the N link to compute in the first step the Josephson CPRs $I(\varphi)$ and obtain in the second step the direction-dependent critical currents necessary to quantify the SDE. In the simultaneous presence of SOI and Zeeman interaction, the bound-state energies depend on φ through $E(\varphi) = \Delta^*(T)f(\varphi)$, where the generic function $f(\varphi)$ is no longer antisymmetric with respect to φ, i.e., $f(-\varphi) \neq f(\varphi)$, reflecting the broken space-inversion and time-reversal symmetries, and the therefrom resulting nontrivial φ_0-phase shifts. Note that the only impact of temperature on $E(\varphi)$ is an effective rescaling (i.e., suppression with increasing temperature) of the superconducting-gap amplitude $\Delta^*(T)$ according to $\Delta^*(T) = \Delta^*(0)\tanh(1.74\sqrt{T_c/T - 1})$, whereas the qualitative shape of $E(\varphi)$ is not altered by temperature. The total Josephson current is then given by

$$I(\varphi) = \sum_E I\big(E(\varphi); T = 0\big)\tanh\left(\frac{E(\varphi)}{2k_BT} \right), \quad (5)$$

where the sum ensures to account for the current contributions of all bound states (i.e., from all transverse channels of the

junction) and k_B indicates the Boltzmann constant. The current at zero temperature can, in the simplest case, be extracted from the thermodynamic relation [73]

$$I\big(E(\varphi); T = 0\big) = -\frac{e}{\hbar} \frac{\partial E(\varphi)}{\partial \varphi} \qquad (6)$$

with the positive elementary charge e. The major temperature effect on the Josephson current originates therefore from the suppression of the higher-harmonic contributions in Eq. (6) due to the tanh term in Eq. (5).

The strengths of the Rashba SOI, the scalar (barrier), and the Zeeman potentials are measured by the dimensionless parameters $\lambda_{\mathrm{SOI}} = m\alpha_R/(\hbar^2 k_F)$, $Z = 2mV_0 d/(\hbar^2 k_F)$, and $\lambda_Z = 2mV_Z d/(\hbar^2 k_F)$, respectively, where $k_F = \sqrt{2m\mu}/\hbar$ refers to the Fermi wave vector (for the experimental parameters, $k_F \approx 3 \times 10^8 \, \mathrm{m}^{-1}$). In agreement with our earlier studies [27, 60], we assume $Z = 0.5$—mimicking an average junction transparency of $\overline{\tau} = 1/[1 + (Z/2)^2] \approx 0.94$—and $\lambda_{\mathrm{SOI}} = 0.661$—corresponding to Rashba SOI $\alpha_R \approx 15 \, \mathrm{meV\,nm}$. For a typical g-factor of $|g^*| \approx 12$, the Zeeman parameter $\lambda_Z = -0.40$ used for our theoretical calculations in the main text corresponds to the magnetic field $B_y \approx -100 \, \mathrm{mT}$.

V. AUTHOR CONTRIBUTIONS

S.R., T.A., and J.B fabricated the devices and performed initial transport characterization of the hybrid superconductor/semiconductor wafer. S.R. and T.A. performed the measurements with the SQUID device. S.R., C.S. and N.P. conceived the experiment. A.C., D.K., and J.F. formulated the theoretical model. A.C. performed the numerical simulations of the temperature dependence of the SDE and φ_0. N.P., S.R., C.S., A.C., and D.K. wrote the manuscript. T.L., S.G., and G.C.G. designed the heterostructure and conducted MBE growth. S.R., T.A. and N.P. analyzed the data. M.J.M. supervised research activities at Purdue.

VI. COMPETING INTERESTS

The authors declare no competing interests.
VII. CODE AVAILABILITY

The computer codes that support the theoretical results, the plots within this paper and other findings of this study are available from the corresponding author upon reasonable request.

[1] R. Winkler, *Spin-orbit Coupling Effects in Two-Dimensional Electron and Hole Systems*, Physics and Astronomy Online Library No. no. 191 (Springer, 2003).

[2] A. Manchon, H. C. Koo, J. Nitta, S. M. Frolov, and R. A. Duine, New perspectives for Rashba spin–orbit coupling, Nature Materials **14**, 871 (2015).

[3] M. Smidman, M. B. Salamon, H. Q. Yuan, and D. F. Agterberg, Superconductivity and spin–orbit coupling in non-centrosymmetric materials: a review, Reports on Progress in Physics **80**, 036501 (2017).

[4] M. Sato and Y. Ando, Topological superconductors: a review, Reports on Progress in Physics **80**, 076501 (2017).

[5] N. F. Q. Yuan and L. Fu, Topological metals and finite-momentum superconductors, Proceedings of the National Academy of Sciences **118**, e2019063118 (2021), https://www.pnas.org/doi/pdf/10.1073/pnas.2019063118.

[6] S. Hart, H. Ren, M. Kosowsky, G. Ben-Shach, P. Leubner, C. Brüne, H. Buhmann, L. W. Molenkamp, B. I. Halperin, and A. Yacoby, Controlled finite momentum pairing and spatially varying order parameter in proximitized HgTe quantum wells, Nature Physics **13**, 87 (2017).

[7] A. Q. Chen, M. J. Park, S. T. Gill, Y. Xiao, D. Reig-i Plessis, G. J. MacDougall, M. J. Gilbert, and N. Mason, Finite momentum Cooper pairing in three-dimensional topological insulator Josephson junctions, Nature Communications **9**, 3478 (2018).

[8] V. M. Edelstein, The Ginzburg - Landau equation for superconductors of polar symmetry, Journal of Physics: Condensed Matter **8**, 339 (1996).

[9] L. Fuchs, D. Kochan, J. Schmidt, N. Hüttner, C. Baumgartner, S. Reinhardt, S. Gronin, G. C. Gardner, T. Lindemann, M. J. Manfra, C. Strunk, and N. Paradiso, Anisotropic Vortex Squeezing in Synthetic Rashba Superconductors: A Manifestation of Lifshitz Invariants, Phys. Rev. X **12**, 041020 (2022).

[10] D. Kochan, A. Costa, I. Zhumagulov, and I. Žutić, Phenomenological Theory of the Supercurrent Diode Effect: The Lifshitz Invariant (2023), arXiv:2303.11975 [cond-mat.supr-con].

[11] J. M. Lu, O. Zheliuk, I. Leermakers, N. F. Q. Yuan, U. Zeitler, K. T. Law, and J. T. Ye, Evidence for two-dimensional Ising superconductivity in gated MoS_2, Science **350**, 1353 (2015), https://www.science.org/doi/pdf/10.1126/science.aab2277.

[12] A. Buzdin, Direct Coupling Between Magnetism and Superconducting Current in the Josephson φ_0 Junction, Phys. Rev. Lett. **101**, 107005 (2008).

[13] A. A. Reynoso, G. Usaj, C. A. Balseiro, D. Feinberg, and M. Avignon, Anomalous Josephson Current in Junctions with Spin Polarizing Quantum Point Contacts, Phys. Rev. Lett. **101**, 107001 (2008).

[14] T. Yokoyama, M. Eto, and Y. V. Nazarov, Anomalous Josephson effect induced by spin-orbit interaction and Zeeman effect in semiconductor nanowires, Phys. Rev. B **89**, 195407 (2014).

[15] D. B. Szombati, S. Nadj-Perge, D. Car, S. R. Plissard, E. P. A. M. Bakkers, and L. P. Kouwenhoven, Josephson φ_0-junction in nanowire quantum dots, Nature Physics **12**, 568 (2016).

[16] E. Strambini, A. Iorio, O. Durante, R. Citro, C. Sanz-Fernández, C. Guarcello, I. V. Tokatly, A. Braggio, M. Rocci, N. Ligato, V. Zannier, L. Sorba, F. S. Bergeret, and F. Giazotto, A Josephson phase battery, Nature Nanotechnology **15**, 656 (2020).

[17] F. Ando, Y. Miyasaka, T. Li, J. Ishizuka, T. Arakawa, Y. Shiota, T. Moriyama, Y. Yanase, and T. Ono, Observation of superconducting diode effect, Nature **584**, 373 (2020).

[18] C. Baumgartner, L. Fuchs, A. Costa, S. Reinhardt, S. Gronin, G. C. Gardner, T. Lindemann, M. J. Manfra, P. E. Faria Junior, D. Kochan, J. Fabian, N. Paradiso, and C. Strunk, Supercurrent rectification and magnetochiral effects in symmetric Josephson junctions, Nature Nanotechnology **17**, 39 (2022).

[19] H. Wu, Y. Wang, Y. Xu, P. K. Sivakumar, C. Pasco, U. Filippozzi, S. S. P. Parkin, Y.-J. Zeng, T. McQueen, and M. N. Ali, The field-free Josephson diode in a van der Waals heterostructure, Nature **604**, 653 (2022).

[20] J. Díez-Mérida, A. Díez-Carlón, S. Y. Yang, Y.-M. Xie, X.-J. Gao, J. Senior, K. Watanabe, T. Taniguchi, X. Lu, A. P. Higginbotham, K. T. Law, and D. K. Efetov, Symmetry-broken josephson junctions and superconducting diodes in magic-angle twisted bilayer graphene, Nature Communications **14**, 2396 (2023).

[21] J.-X. Lin, P. Siriviboon, H. D. Scammell, S. Liu, D. Rhodes, K. Watanabe, T. Taniguchi, J. Hone, M. S. Scheurer, and J. I. A. Li, Zero-field superconducting diode effect in small-twist-angle trilayer graphene, Nature Physics **18**, 1221 (2022).

[22] B. Turini, S. Salimian, M. Carrega, A. Iorio, E. Strambini, F. Giazotto, V. Zannier, L. Sorba, and S. Heun, Josephson diode effect in high-mobility insb nanoflags, Nano Letters **22**, 8502 (2022).

[23] B. Pal, A. Chakraborty, P. K. Sivakumar, M. Davydova, A. K. Gopi, A. K. Pandeya, J. A. Krieger, Y. Zhang, M. Date, S. Ju, N. Yuan, N. B. M. Schröter, L. Fu, and S. S. P. Parkin, Josephson diode effect from Cooper pair momentum in a topological semimetal, Nature Physics 10.1038/s41567-022-01699-5 (2022).

[24] K.-R. Jeon, J.-K. Kim, J. Yoon, J.-C. Jeon, H. Han, A. Cottet, T. Kontos, and S. S. P. Parkin, Zero-field polarity-reversible Josephson supercurrent diodes enabled by a proximity-magnetized Pt barrier, Nature Materials **21**, 1008 (2022).

[25] N. Lotfizadeh, B. Pekerten, P. Yu, W. Strickland, A. Matos-Abiague, and J. Shabani, Superconducting Diode Effect Sign Change in Epitaxial Al-InAs Josepshon Junctions (2023), arXiv:2303.01902 [cond-mat.mes-hall].

[26] G. P. Mazur, N. van Loo, D. van Driel, J. Y. Wang, G. Badawy, S. Gazibegovic, E. P. A. M. Bakkers, and L. P. Kouwenhoven, The gate-tunable Josephson diode (2022), arXiv:2211.14283 [cond-mat.supr-con].

[27] A. Costa, C. Baumgartner, S. Reinhardt, J. Berger, S. Gronin, G. C. Gardner, T. Lindemann, M. J. Manfra, J. Fabian, D. Kochan, N. Paradiso, and C. Strunk, Sign reversal of the Josephson inductance magnetochiral anisotropy and 0–π-like transitions in supercurrent diodes, Nature Nanotechnology 10.1038/s41565-023-01451-x (2023).

[28] L. Bauriedl, C. Bäuml, L. Fuchs, C. Baumgartner, N. Paulik, J. M. Bauer, K.-Q. Lin, J. M. Lupton, T. Taniguchi, K. Watanabe, C. Strunk, and N. Paradiso, Supercurrent diode effect and magnetochiral anisotropy in few-layer NbSe2, Nature Communications **13**, 4266 (2022).

[29] J. Yun, S. Son, J. Shin, G. Park, K. Zhang, Y. J. Shin, J.-G. Park, and D. Kim, Magnetic proximity-induced superconducting diode effect and infinite magnetoresistance in a van der Waals heterostructure, Phys. Rev. Res. **5**, L022064 (2023).

[30] A. Banerjee, M. Geier, M. A. Rahman, C. Thomas, T. Wang, M. J. Manfra, K. Flensberg, and C. M. Marcus, Phase Asymmetry of Andreev Spectra From Cooper-Pair Momentum (2023), arXiv:2301.01881 [cond-mat.supr-con].

[31] A. Sundaresh, J. I. Väyrynen, Y. Lyanda-Geller, and L. P. Rokhinson, Diamagnetic mechanism of critical current non-reciprocity in multilayered superconductors, Nature Communications **14**, 1628 (2023).

[32] A. Assouline, C. Feuillet-Palma, N. Bergeal, T. Zhang, A. Mottaghizadeh, A. Zimmers, E. Lhuillier, M. Eddrie, P. Atkinson, M. Aprili, and H. Aubin, Spin-Orbit induced phase-shift in Bi2Se3 Josephson junctions, Nature Communications **10**, 126 (2019).

[33] W. Mayer, M. C. Dartiailh, J. Yuan, K. S. Wickramasinghe, E. Rossi, and J. Shabani, Gate controlled anomalous phase shift in Al/InAs Josephson junctions, Nature Communications **11**, 212 (2020).

[34] M. C. Dartiailh, W. Mayer, J. Yuan, K. S. Wickramasinghe, A. Matos-Abiague, I. Žutić, and J. Shabani, Phase Signature of Topological Transition in Josephson Junctions, Phys. Rev. Lett. **126**, 036802 (2021).

[35] B. Zhang, Z. Li, V. Aguilar, P. Zhang, M. Pendharkar, C. Dempsey, J. S. Lee, S. D. Harrington, S. Tan, J. S. Meyer, M. Houzet, C. J. Palmstrom, and S. M. Frolov, Evidence of φ_0-Josephson junction from skewed diffraction patterns in Sn-InSb nanowires (2022), arXiv:2212.00199 [cond-mat.supr-con].

[36] D. Z. Haxell, M. Coraiola, D. Sabonis, M. Hinderling, S. C. ten Kate, E. Cheah, F. Krizek, R. Schott, W. Wegscheider, and F. Nichele, Zeeman and orbital driven phase transitions in planar josephson junctions (2023), arXiv:2306.01514 [cond-mat.supr-con].

[37] I. V. Krive, L. Y. Gorelik, R. I. Shekhter, and M. Jonson, Chiral symmetry breaking and the Josephson current in a ballistic superconductor–quantum wire–superconductor junction, Low Temperature Physics **30**, 398 (2004), https://pubs.aip.org/aip/ltp/article-pdf/30/5/398/8232439/398_1_online.pdf.

[38] A. Barone and G. Paterno, *Physics and Applications of the Josephson Effect*, 2nd ed. (John Wiley and Sons, Inc., 1982).

[39] H. F. Legg, K. Laubscher, D. Loss, and J. Klinovaja, Parity protected superconducting diode effect in topological josephson junctions (2023), arXiv:2301.13740 [cond-mat.mes-hall].

[40] F. Pientka, A. Keselman, E. Berg, A. Yacoby, A. Stern, and B. I. Halperin, Topological superconductivity in a planar josephson junction, Phys. Rev. X **7**, 021032 (2017).

[41] B. Scharf, F. Pientka, H. Ren, A. Yacoby, and E. M. Hankiewicz, Tuning topological superconductivity in phase-controlled Josephson junctions with Rashba and Dresselhaus spin-orbit coupling, Phys. Rev. B **99**, 214503 (2019).

[42] A. Daido, Y. Ikeda, and Y. Yanase, Intrinsic superconducting diode effect, Phys. Rev. Lett. **128**, 037001 (2022).

[43] N. F. Q. Yuan and L. Fu, Supercurrent diode effect and finite-momentum superconductors, Proceedings of the National Academy of Sciences **119**, e2119548119 (2022), https://www.pnas.org/doi/pdf/10.1073/pnas.2119548119.

[44] J. J. He, Y. Tanaka, and N. Nagaosa, A phenomenological theory of superconductor diodes, New Journal of Physics **24**, 053014 (2022).

[45] S. Ilić and F. S. Bergeret, Theory of the Supercurrent Diode Effect in Rashba Superconductors with Arbitrary Disorder, Phys. Rev. Lett. **128**, 177001 (2022).

[46] J.-X. Hu, Z.-T. Sun, Y.-M. Xie, and K. T. Law, Josephson Diode Effect Induced by Valley Polarization in Twisted Bilayer Graphene, Phys. Rev. Lett. **130**, 266003 (2023).

[47] R. Grein, M. Eschrig, G. Metalidis, and G. Schön, Spin-dependent cooper pair phase and pure spin supercurrents in strongly polarized ferromagnets, Phys. Rev. Lett. **102**, 227005 (2009).

[48] Y. Zhang, Y. Gu, P. Li, J. Hu, and K. Jiang, General Theory of Josephson Diodes, Phys. Rev. X **12**, 041013 (2022).

[49] H. D. Scammell, J. I. A. Li, and M. S. Scheurer, Theory of zero-field superconducting diode effect in twisted trilayer graphene, 2D Materials **9**, 025027 (2022).

[50] M. Davydova, S. Prembabu, and L. Fu, Universal josephson diode effect, Science Advances **8**, eabo0309 (2022), https://www.science.org/doi/pdf/10.1126/sciadv.abo0309.

[51] P.-H. Fu, Y. Xu, C. H. Lee, S. A. Yang, Y. S. Ang, and J.-F. Liu, Field-Effect Josephson Diode via Asymmetric Spin-Momentum Locking States (2023), arXiv:2212.01980 [cond-mat.mes-hall].

[52] B. Lu, S. Ikegaya, P. Burset, Y. Tanaka, and N. Nagaosa, Josephson diode effect on the surface of topological insulators (2022), arXiv:2211.10572 [cond-mat.supr-con].

[53] A. Costa, J. Fabian, and D. Kochan, Microscopic study of the Josephson supercurrent diode effect in 2DEG-based Josephson junctions (2023), arXiv:2303.14823 [cond-mat.supr-con].

[54] A. Fornieri, A. M. Whiticar, F. Setiawan, E. Portolés, A. C. C. Drachmann, A. Keselman, S. Gronin, C. Thomas, T. Wang, R. Kallaher, G. C. Gardner, E. Berg, M. J. Manfra, A. Stern, C. M. Marcus, and F. Nichele, Evidence of topological superconductivity in planar josephson junctions, Nature **569**, 89 (2019).

[55] A. Banerjee, O. Lesser, M. A. Rahman, H. R. Wang, M. R. Li, A. Kringhøj, A. M. Whiticar, A. C. C. Drachmann, C. Thomas, T. Wang, M. J. Manfra, E. Berg, Y. Oreg, A. Stern, and C. M. Marcus, Signatures of a topological phase transition in a planar Josephson junction (2022), arXiv:2201.03453.

[56] C. Baumgartner, L. Fuchs, A. Costa, J. Picó-Cortés, S. Reinhardt, S. Gronin, G. C. Gardner, T. Lindemann, M. J. Manfra, P. E. F. Junior, D. Kochan, J. Fabian, N. Paradiso, and C. Strunk, Effect of Rashba and Dresselhaus spin–orbit coupling on supercurrent rectification and magnetochiral anisotropy of ballistic Josephson junctions, Journal of Physics: Condensed Matter **34**, 154005 (2022).

[57] F. Nichele, E. Portolés, A. Fornieri, A. M. Whiticar, A. C. C. Drachmann, S. Gronin, T. Wang, G. C. Gardner, C. Thomas, A. T. Hatke, M. J. Manfra, and C. M. Marcus, Relating Andreev Bound States and Supercurrents in Hybrid Josephson Junctions, Phys. Rev. Lett. **124**, 226801 (2020).

[58] J. Shabani, M. Kjaergaard, H. J. Suominen, Y. Kim, F. Nichele, K. Pakrouski, T. Stankevic, R. M. Lutchyn, P. Krogstrup, R. Feidenhans'l, S. Kraemer, C. Nayak, M. Troyer, C. M. Marcus, and C. J. Palmstrøm, Two-dimensional epitaxial superconductor-semiconductor heterostructures: A platform for topological superconducting networks, Phys. Rev. B **93**, 155402 (2016).

[59] K. S. Wickramasinghe, W. Mayer, J. Yuan, T. Nguyen, L. Jiao, V. Manucharyan, and J. Shabani, Transport properties of near surface InAs two-dimensional heterostructures, Applied Physics Letters **113**, 262104 (2018), https://pubs.aip.org/aip/apl/article-pdf/doi/10.1063/1.5050413/14521159/262104_1_online.pdf.

[60] C. Baumgartner, L. Fuchs, L. Frész, S. Reinhardt, S. Gronin, G. C. Gardner, M. J. Manfra, N. Paradiso, and C. Strunk, Josephson Inductance as a Probe for Highly Ballistic Semiconductor-Superconductor Weak Links, Phys. Rev. Lett. **126**, 037001 (2021).

[61] T. Zhang, T. Lindemann, G. C. Gardner, S. Gronin, T. Wu, and M. J. Manfra, Mobility exceeding 100 000 cm^2/V s in modulation-doped shallow InAs quantum wells coupled to epitaxial aluminum, Phys. Rev. Mater. **7**, 056201 (2023).

[62] M. Tinkham, *Introduction to Superconductivity: Second Edition (Dover Books on Physics) (Vol i)*, 2nd ed. (Dover Publications, 2004).

[63] S. Goswami, E. Mulazimoglu, A. M. R. V. L. Monteiro, R. Wölbing, D. Koelle, R. Kleiner, Y. M. Blanter, L. M. K. Vandersypen, and A. D. Caviglia, Quantum interference in an interfacial superconductor, Nature Nanotechnology **11**, 861 (2016).

[64] J. R. McLaughlan, E. M. Llewellyn-Samuel, and S. Crampin, Spin–orbit splitting of image states, Journal of Physics: Condensed Matter **16**, 6841 (2004).

[65] Y. Gindikin and V. A. Sablikov, Image-potential-induced spin-orbit interaction in one-dimensional electron systems, Phys. Rev. B **95**, 045138 (2017).

[66] T. Nakazawa, N. Takagi, M. Kawai, H. Ishida, and R. Arafune, Rashba splitting in an image potential state investigated by circular dichroism two-photon photoemission spectroscopy, Phys. Rev. B **94**, 115412 (2016).

[67] Max Geier, Karsten Flensberg, private communication.

[68] P. A. Volkov, Étienne Lantagne-Hurtubise, T. Tummuru, J. H. Pixley, S. Plugge, and M. Franz, Josephson diode effects in twisted nodal superconductors (2023), arXiv:2307.01261 [cond-mat.supr-con].

[69] P. Virtanen and T. T. Heikkilä, Nonreciprocal Josephson linear response (2023), arXiv:2306.12295 [cond-mat.supr-con].

[70] C. Leroux, A. Parra-Rodriguez, R. Shillito, A. Di Paolo, W. D. Oliver, C. M. Marcus, M. Kjaergaard, A. Gyenis, and A. Blais, Nonreciprocal devices based on voltage-tunable junctions (2022), arXiv:2106.03575.

[71] P. G. De Gennes, *Superconductivity of Metals and Alloys* (Addison Wesley, Redwood City, 1989).

[72] A. F. Andreev, Electron Spectrum of the Intermediate State of Superconductors, Zh. Eksp. Teor. Fiz. **49**, 655 (1966); J. Exp. Theor. Phys. **22**, 455 (1966).

[73] I. O. Kulik, Macroscopic Quantization and the Proximity Effect in S-N-S Junctions, Zh. Eksp. Teor. Fiz. **57**, 1745 (1969); J. Exp. Theor. Phys. **30**, 944 (1970).

[74] J. Yuan, M. Hatefipour, B. A. Magill, W. Mayer, M. C. Dartiailh, K. Sardashti, K. S. Wickramasinghe, G. A. Khodaparast, Y. H. Matsuda, Y. Kohama, Z. Yang, S. Thapa, C. J. Stanton, and J. Shabani, Experimental measurements of effective mass in near-surface inas quantum wells, Phys. Rev. B **101**, 205310 (2020).

[75] G. L. J. A. Rikken, J. Fölling, and P. Wyder, Electrical Magnetochiral Anisotropy, Phys. Rev. Lett. **87**, 236602 (2001).

Supplementary Information

Link between supercurrent diode and anomalous Josephson effect revealed by gate-controlled interferometry

VIII.   WAFER GROWTH AND SAMPLE FABRICATION

The hybrid superconductor-semiconductor layer stack is shown in Fig. S1**a**. The active layer consists of a bottom barrier of 4 nm $In_{0.75}Ga_{0.25}As$, a 7 nm InAs quantum well, and a top barrier of 10 nm $In_{0.75}Ga_{0.25}As$. Growth of the semiconductor stack is followed by in-situ deposition of 5 nm aluminum [61].

The mesa of the SQUID device is wet etched using a solution of H_3PO_4:$C_6H_8O_7$:H_2O_2:H_2O (1.2:14:2:88) to a depth of 250 nm. The Josephson junctions are defined using standard electron beam lithography. Prior to etching of the junctions, we expose the developed structures to oxygen plasma for 5 s in order to remove residues of PMMA resist. Selective etching of the aluminum in the junctions is then performed with aluminum etchant type D from Transene at 50 °C for 3 s. Both junctions are covered with 60 nm aluminum oxide grown by atomic layer deposition at 80 °C. Before the first pulse (trimethylaluminum), the sample is dried under nitrogen flow for 2 hours. Finally, a Ti/Au (5 nm / 100 nm) top-gate is deposited onto JJ2 by electron beam evaporation.

IX.   BASIC CHARACTERISATION OF THE QUANTUM WELL AND THE SUPERCONDUCTOR

Basic transport properties of the semiconductor quantum well are performed with a standard Hall bar device. The aluminum film is removed from the Hall bar and a top-gate is fabricated using the methods described above. In Figures S1**b-e** we show Hall mobility, mean free path, Fermi wavelength, and Fermi velocity as a function of carrier density at $T = 1.5$ K. The peak mobility $\mu > 60000$ cm^2/Vs is obtained at the density $n \sim 5 \times 10^{11}$ cm^{-2}.

The electron effective mass is determined from the temperature dependence of Shubnikov-de Haas (SdH) oscillations, following [74]. Figure S1**f** shows SdH oscillations in the resistance with a second-order polynomial background removed in order to obtain the amplitude of each oscillation as a function of temperature. The carrier density obtained from the oscillations is $\sim 7 \times 10^{11}$ cm^{-2}. For each maximum and minimum of the oscillations we obtain an effective mass by fitting the temperature dependence of the amplitude with the formula

$$A_{\text{SdH}}(T) \sim \frac{2\pi^2 k_B T/\hbar\omega_c}{\sinh(2\pi^2 k_B T/\hbar\omega_c)} \tag{S.7}$$

The obtained mass $m^*/m_e = 0.036 \pm 0.005$ is slightly lower compared to the value $m^*/m_e = 0.04$ found in [74].

Figures S1**g** shows the resistance of the heterostructure, including the aluminum film, as a function of temperature, measured in a Hall bar geometry. Due to the low thickness of the film, the critical temperature is enhanced to 2.07 K with a normal state sheet resistance of 36 Ω.

X.   MEASUREMENT TECHNIQUES AND DATA EVALUATION

Measurements are performed in a dilution cryostat with a base temperature of 40 mK. Differential resistance $dV/dI(I_{DC})$ is measured in a standard 4-point setup using a current excitation of $I_{ac} = 10$ nA(rms) at frequency $f = 2.333$ kHz. The voltage is measured using a differential bipolar junction preamplifier (SR552) and a digital lock-in amplifier (SR830). All measurement lines are filtered at the head of the cryostat using LC filters (Tusonix 4201-053). Below the mixing chamber we use highly resistive CuNi/CuNi coaxial lines (GVLZ185) with a large attenuation above 100 MHz. The fields B_z and B_y are applied using a 2-axis vector magnet, and the rotation of the in-plane field is performed by mounting the sample on an Attocube piezo rotator (ANRv220). A resolution below 50 nT in B_z is realized by exchanging the magnet power supply with a high precision current source (Keysight B2961B). Before starting a measurement at a new configuration of in-plane field and/or rotation angle we heat our sample above the critical temperature $T_c \sim 2K$ and perform a field cooling in zero out-of-plane field. The gate voltage V_g is applied using a source meter (Keysight B2901B). For gate voltages in the range $V_g = -2.5$ V...1 V the leakage current is below the resolution of the instrument ($|I_{\text{leak}}| < 1$ pA). For the definition of the SQUID critical current we use a threshold resistivity of $dV/dI = 6$ Ω. Using a different definition for the threshold has no visible effect on the results.

For the determination of φ_0 and η the SQUID critical current $I_c(B_z)$ is measured for the sequence of gate voltages $V_g = -2.5$ V, -1.5 V, ..., 0.5 V, 1 V. The accuracy is improved by repeatedly cycling the gate voltage through this sequence (40 cycles for most measurements). After obtaining φ_0 and η we average over all cycles. The error bars in Fig. 2**e** for the values of η are found as the standard error of the mean.
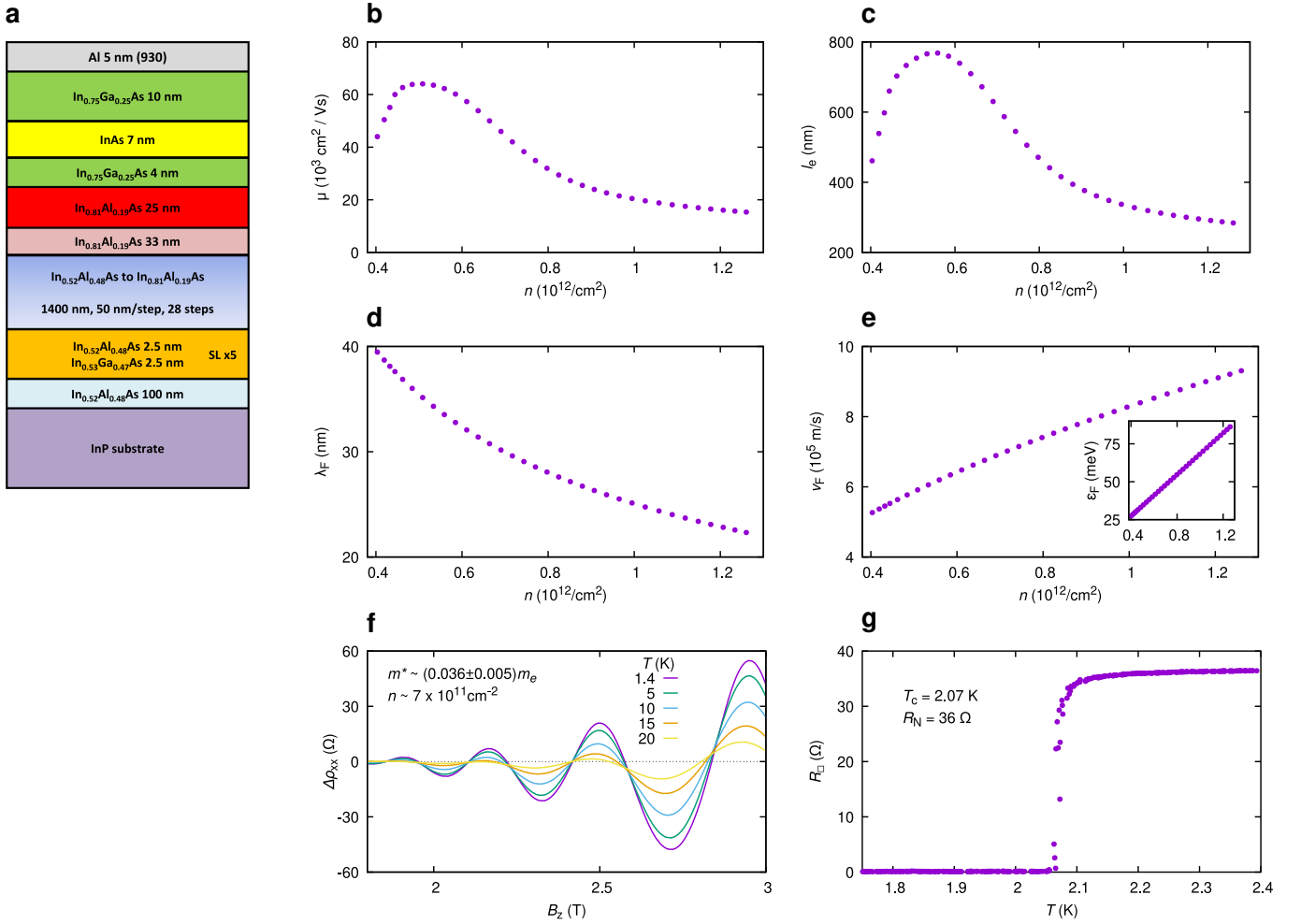
FIG. S1. **a**, Layer stack of the used wafer. **b-e**, Transport properties of the quantum well measured with a top gated Hall bar at temperature $T = 1.5$ K. The inset of panel **e** shows the Fermi level ε_F versus n. The range in gate voltage corresponding to the n-range displayed in panels **b-e** is [-3.5 V,-0.2 V]. **f**, Amplitude of Shubnikov-de Haas oscillations for temperatures between 1.4 K and 20 K. **g** $R(T)$ Characteristic of a Hall bar device with the pristine aluminum film.

XI. MODELING OF INDUCTIVE SCREENING EFFECTS IN THE ASYMMETRIC SQUID

The obtained critical currents of the SQUID device are strongly affected by the large kinetic inductance of the aluminum electrodes. A minimal circuit model of our device, which includes the inductance of the electrodes of JJ1 and the loop, is show in Figure S2**a**. The reference junction JJ1 is modeled as a network of N JJs in parallel, each with critical current $I_{c,1}/N$. Setting $N = 20$ is sufficient to model the central lobe of the Fraunhofer interference pattern of JJ1. The effective area of JJ1 is A_{ref}, while the area of the large loop is A_{loop}. The positive and negative critical currents for a given out-of-plane field B_z can be calculated as a function of the phase difference γ_{JJ2} over JJ2. Given γ_{JJ2} the phase difference $\gamma_{\mathrm{JJ1,N}}$ over the rightmost junction in JJ1 is

$$\gamma_{\mathrm{JJ1},N} = \gamma_{\mathrm{JJ2}} - 2\pi(B_z A_{\mathrm{loop}} - L_{\mathrm{loop}}I_{c,2}\sin(\gamma_{\mathrm{JJ2}}))/\Phi_0 \tag{S.8}$$

The phase differences $\gamma_{\mathrm{JJ1},i}$ are found by iteration:

$$\gamma_{\mathrm{JJ1},i} = \gamma_{\mathrm{JJ1},i} - 2\pi(B_z A_{\mathrm{ref}}/(N-1) - L_{\mathrm{ref}}/(N-1)I_{i+1})/\Phi_0 \tag{S.9}$$

where $I_i = I_{i+1} + I_{c,1}/N\sin(\gamma_{\mathrm{JJ1},i+1})$ is the current flowing through the inductor between junctions i and $i + 1$. The positive and negative critical currents are then found as the extremal values of $I_0(\gamma_{\mathrm{JJ2}})$. In FiguresS2**b-d** we model the SQUID critical current obtained for a in-plane-field $|B_y| = 100$ mT. A good match to the data can be found with the following parameters: $A_{\mathrm{loop}} = 1150$ (µm)^2, $I_{c,1} = 2.48\ \mu$A, $A_{\mathrm{ref}} = 70$ (µm)^2, $L_{\mathrm{ref}} = 0.8$ nH, and $L_{\mathrm{loop}} = 1.5$ nH. From the value of L_{loop} we determine the sheet inductance of the aluminum film $L_{\square} = L_{\mathrm{loop}}/N_{\square,\mathrm{loop}} = 1.5$ nH/46 $\sim$ 30 pH. The kinetic inductance of the loop largely exceeds the geometric inductance which we estimate as $L_{\mathrm{loop,geo}} \lesssim 100$ pH.

The amplitude of the SQUID oscillations at $V_g = 1$ V, $By = -100$ mT and $T = 40$ mK is matched by setting $I_{c,2} = 400$ nA. Figure S2**b** shows the SQUID critical current for different values of $I_{c,2}$ near the maximum of the SQUID critical current. Importantly, the crossing point with the reference line ($I_{c,2} = 0$) is the same for all values of $I_{c,2}$, showing that screening has no effect on our evaluation of $\Delta\varphi_0$.

Figure S2**c** shows the results of SQUID oscillation measurements performed for $V_g = 1.0$ V (green) and $V_g = -2.5$ V (purple), at $B_y = -100$ mT and $T = 40$ mK. A comparison with the results of our calculations in Fig. S2**d** makes it evident that our simple model described above correctly captures the behavior of the SQUID. We want to stress that our asymmetric SQUID displays a trivial supercurrent diode behavior (in Fig. S2**c,d** in general $I_c^+(B_z) \neq I_c^-(B_z)$). This is a long known feature of asymmetric SQUIDs and it is not the focus of our work. Instead, our focus is on the physics of a single, homogeneous Josephson junction (JJ2).

From the analysis of the inductive screening effects discussed above, we can conclude that:

- Owing to screening effects, the SQUID oscillations do not reproduce the CPR of JJ2. However, for positive bias, one can still deduce $I_{c,2}^+$ from the maximum of the oscillations, since these two quantities are proportional, see Fig. S2**d**. Instead, **for positive bias, one cannot deduce $I_{c,2}^-$ from the minima of the SQUID oscillations**. The correct way to deduce $I_{c,2}^-$ is to look at oscillations for negative current bias. $I_{c,2}^-$ is proportional to the **minima** of the SQUID oscillations for **negative bias**, see Fig. 2**c** of the main text.

- As it is clearly visible in Figures S2**c,d**, the amplitudes of the fast SQUID oscillations are not constant. This is caused by a coupling of the loop current I_{JJ2} to the flux of JJ1. The flux in JJ1 is changed by $\Phi \sim L_{\text{ref}}I_{JJ2}$, modulating the critical current of JJ1. For the measurement of critical currents, demonstrated in Figure 2 of the main text, we find that the critical currents for different gate voltages are only proportional to $I_{c,2}(V_g)$, with the proportionality constant depending on the chosen SQUID oscillation (i.e., on the exact B_z value). As positive and negative critical currents need to be measured at opposite current bias (see previous points), the slightly different scale factors result in offsets for the extracted diode efficiency $\eta = 2(I_c^+ - |I_c^-|)/(I_c^+ + |I_c^-|)$. We note that the gate slope $d\eta/dV_g$ is nevertheless a well defined quantity and not affected by the screening effects.

- As a consequence of the B_z-dependence of the amplitude of the SQUID oscillations, the correct way to compare an oscillation with positive bias with one with negative bias is to consider oscillations with opposite B_z, namely oscillations which are inversion-symmetric around the origin of the $I_c(B_z)$ graph, see arrows in Fig. 2**a** of the main text. Indeed, by the global time-reversal symmetry $I_c^+(B_z) = -I_c^-(-B_z)$ in absence of in-plane field. Taking precisely opposite oscillations, as described in the previous point, should make screening effect irrelevant, so that, in principle, the observation of finite η for finite B_{ip} should be considered as a real effect and not an artifact of screening. However, the combination of φ_0-shift and the strong dependence of the SQUID oscillations on B_z makes it possible to measure (following the aforementioned procedure) a finite η even in absence of a genuine SDE in JJ2. In fact, owing to the finite φ_0, opposite SQUID oscillations do not occur anymore at exactly opposite B_z, and the strong B_z dependence of the SQUID oscillations can render the opposite oscillation amplitudes not exactly equal even in absence of intrinsic SDE. The effect is very small, still we maintained a conservative approach and decided to look at $\partial\eta/\partial V_g$ instead of η itself. Also, we can exclude that the gate dependence of η is a simple artifact of that of φ_0 (due to the mechanism just described) for the following reasons: (i) from our calculations the measured η is too large to be entirely generated by the mechanism just described (φ_0 plus B_z-dependent oscillations). (ii) The gate dependence of φ_0 and η are different: the former is nonlinear, the latter is linear (compare Fig. 1**g** and Fig. 2**e** of the main text). (iii) The temperature dependence of $\Delta\varphi_0$ and that of $\partial\eta/\partial V_g$ is dramatically different, see Fig. 3 of the main text.

- From Fig. S2**b** we can conclude that inductive screening does not affect the value of B_z at which $I_2 = 0$ (the curves all cross the baseline at the same point). Clearly, for positive bias, it is important to only consider the crossing with the baseline *with positive slope*, which is the significant one. This explains our operational definition of B_0, which is important to determine φ_0.

- The inductive screening effects depend on the kinetic inductance of the Al film and on the magnitude of the supercurrent flowing the in the SQUID arms. By increasing B_{ip} in the range under study, the decrease of the critical current I_c is more important than the increase of the kinetic inductance of the arms. Therefore, the larger B_{ip}, the smaller the impact of screening. Since φ_0 measurements are more sensitive to inductive screening, we were able to extract $\Delta\varphi_0$ only for $B_{\text{ip}} \geq 100$ mT.

XII. GATE DEPENDENCE OF THE MAGNETOCHIRAL ANISOTROPY FOR THE INDUCTANCE

In this section we comment about the gate dependence of the magnetochiral anisotropy (MCA) of the inductance, which we measured in our previous work, Ref. [18]. In that work, we established an analogy between the known MCA for the resistance
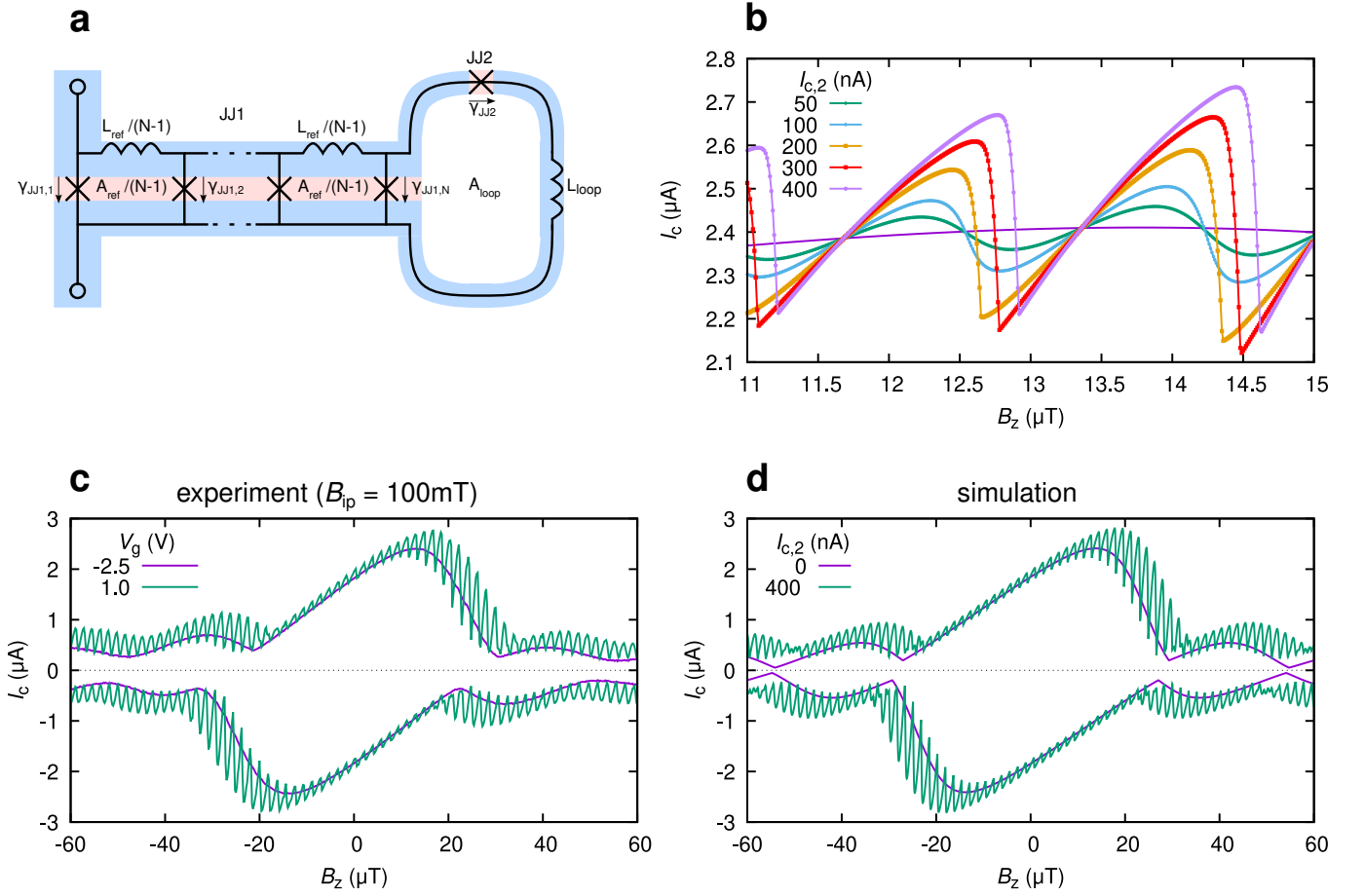
FIG. S2. **a**, Minimal circuit model of the SQUID device. **b,d**, Simulated critical currents of the SQUID with parameters as described in the text. **c**, experimental values of positive and negative critical currents for $B_{\mathrm{ip}} = 100$ mT and $\theta = -90\,^\circ$.

(e.g. in the fluctuation regime of a noncentrosymmetric superconductor) and MCA for the inductance. This latter was the new quantity introduced in Ref. [18], where we showed that the Josephson inductance can be written as

$$L = L_0[1 + \gamma_L \hat{e}_z \cdot (\vec{B} \times \vec{I})], \tag{S.10}$$

where $\gamma_L \equiv 2L_0'/(L_0 B_{ip})$, with $L_0' \equiv \frac{dL}{dI}|_{I=0}$. Equation S.10 mirrors the Rikken formula [75]

$$R = R_0[1 + \gamma \hat{e}_z \cdot (\vec{B} \times \vec{I})], \tag{S.11}$$

which holds for noncentrosymmetric conductors with nonreciprocal resistance, for which γ is defined as $2R_0'/(R_0 B_{ip})$, with $R_0' \equiv \frac{dR}{dI}|_{I=0}$.

It must be kept in mind that both the MCA coefficient for the resistance (γ) and that for the inductance (γ_L) are dimensional quantities which scale with the inverse of the sample width in quasi 2D conductors. In Ref. [18], we have plotted in Fig. 2d the gate dependence γ_L. At first glance, it might appear that no dependence is observed (the curves in Fig. 2d of Ref. [18] fall on top of each other). However, it must be kept in mind that γ_L trivially depends on the number of channels N (or, equivalently, on the width). Since $I \propto N$ and $L_0 \propto N^{-1}$, then γ_L must scale as $1/N$. Therefore, in Ref. [18] the fact that γ_L appears constant is due to the fact that the expected increase of the specific magnetochiral character (considered "per channel") is compensated by the decrease due to the trivial increase of N (decrease of N^{-1}).

The best way to represent the gate-induced enhancement of the MCA for the inductance (which mirrors the increase in $|\varphi_0|$ and η with V_g demonstrated in the present article) is to represent the MCA with a quantity which does not depend on N. To this end, we plot in Fig. S3**a** the V_g dependence of the quantity $\Phi_0|L_0'|/L_0^2$ for the same data set of Fig. 2d in Ref. [18]. Data refer to $B_{\mathrm{ip}} = 100$ mT and $\theta = 90°$ (purple) and $\theta = 270°$ (green). We clearly observe an increase in the magnetochiral character with V_g. The increase is relatively small due to the fact that in that sample the gate had a much weaker effect compared to the sample studied in the present article. To give an idea of this, in Fig. S3**b** we plot L_0 as a function of V_g, showing that sweeping V_g from -1.5 to 0 V corresponds to a change in L_0 of less than 20%.
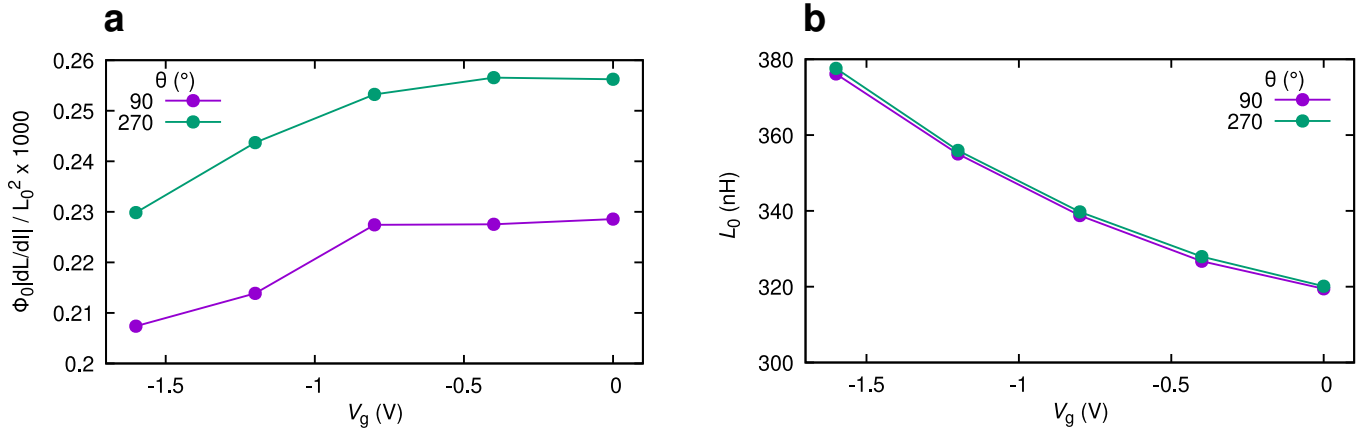
FIG. S3. Magnetochiral anisotropy of the Josephson inductance for 1D array at $B_{\mathrm{ip}} = 100$ mT.
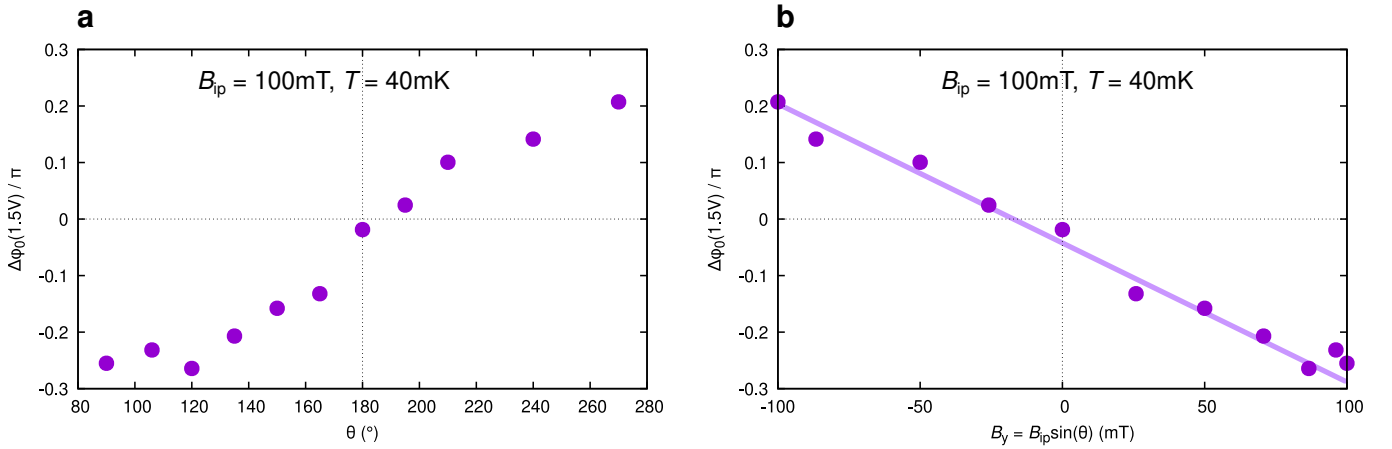
FIG. S4. **a**, Anomalous phase shift for $B_{ip} = 100$ mT as a function of θ as defined in the main text. **b**, Anomalous phase shift as a function of $B_y = B_{ip} \sin(\theta)$.

XIII.   ANGLE DEPENDENCE OF THE ANOMALOUS PHASE SHIFT

Figure S4**a** shows the dependence of the anomalous phase difference $\Delta\varphi_0(V_g = 1.5$ V, $B_{\mathrm{ip}} = 100$ mT) on the rotation angle θ defined in the main text. The observed behaviour is in good agreement with the expected relation $\varphi_0 \sim \sin(\theta)$. In Fig. S4**b** we plot $\Delta\varphi_0$ as a function of the B_y component of the in-plane field ($B_y := B_{ip} \sin(\theta)$), showing a good agreement with the expected linear behaviour.

XIV.   SUPPLEMENTAL DATA ON TEMPERATURE DEPENDENCE

Figure S5**a** shows the temperature dependence of the differential resistance dV/dI of the SQUID for zero DC bias current and zero magnetic field. The positive and negative critical currents $I_{c,2}^{\pm}$ of JJ2 corresponding to Fig. 3**c** and **d** of the main text are shown in Fig. S5**b**. At $T = 750$ mK the critical current is reduced by ~ 50 %. Fig. S5**c** and **d** show $\eta(V_g)$ for the temperatures $T = 40$ mK and $T = 750$ mK (corresponding to the first and last data points in Fig. 3**d** of the main text). At $T = 750$ mK we observe larger statistical errors in the determination of the critical currents, leading to the larger error bars. By increasing the temperature, the superconducting-to-normal transition in the differential resistance becomes less sharp, leading to the increased noise in the determination of critical currents, and thereby the diode efficiency.
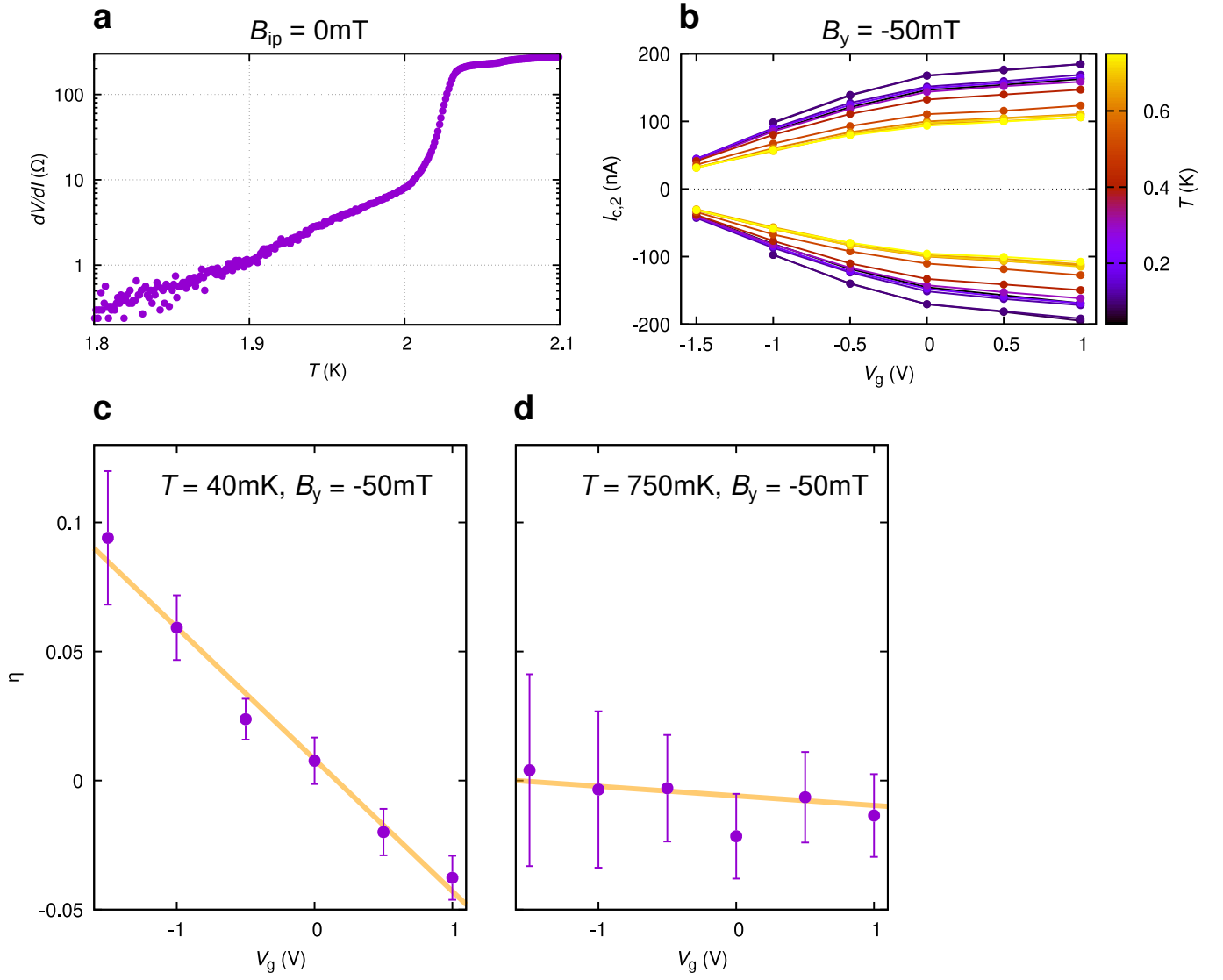
FIG. S5. **a**, $dV/dI(T)$ of the SQUID device at zero DC bias and zero magnetic field. **b**, Critical current $I_{c,2}^{\pm}(V_g)$ at $B_y = -50$ mT for different temperatures. **c** and **d**, Diode efficiency $\eta(V_g)$ for $T = 40$ mK and $T = 750$ mK.